

## **Coherent Anti-Stokes Raman Scattering (CARS) as a Probe for Supersonic Hydrogen-Fuel/Air Mixing**

P. M. Danehy<sup>†</sup>, S. O'Byrne<sup>\*</sup>

*NASA Langley Research Center, Hampton, VA, 23681*

A. D. Cutler

*The George Washington University, MS 905, NASA Langley Research Center, Hampton, VA, 23681*

C. G. Rodriguez

*GASL Inc., MS353X, NASA Langley Research Center, Hampton, VA, 23681*

### **ABSTRACT**

The dual-pump coherent anti-Stokes Raman spectroscopy (CARS) method was used to measure temperature and the absolute mole fractions of N<sub>2</sub>, O<sub>2</sub> and H<sub>2</sub> in a supersonic non-reacting fuel-air mixing experiment. Experiments were conducted in NASA Langley Research Center's Direct Connect Supersonic Combustion Test Facility. Under normal operation of this facility, hydrogen and air burn to increase the enthalpy of the test gas and O<sub>2</sub> is added to simulate air. This gas is expanded through a Mach 2 nozzle and into a combustor model where fuel is then injected, mixes and burns. In the present experiment the O<sub>2</sub> of the test gas is replaced by N<sub>2</sub>. The lack of oxidizer inhibited combustion of the injected H<sub>2</sub> fuel jet allowing the fuel / air mixing process to be studied. CARS measurements were performed 427 mm downstream of the nozzle exit and 260 mm downstream of the fuel injector. Maps were obtained of the mean temperature, as well as the N<sub>2</sub>, O<sub>2</sub> and H<sub>2</sub> mean mole fraction fields. A map of mean H<sub>2</sub>O vapor mole fraction was also inferred from these measurements. Correlations between different measured parameters and their fluctuations are presented. The CARS measurements are compared with a preliminary computational prediction of the flow.

### **INTRODUCTION**

Ensuring adequate fuel-air mixing is a difficult but essential goal that must be achieved to realize hypersonic air-breathing flight. Ambient air ingested by the engine passes through the combustor supersonically. Various injection strategies are used to encourage the fuel to mix with this rapidly moving air so that combustion takes place prior to expanding the gas through the nozzle to extract thrust. Mixing of fuel and air, combined with ignition delays associated with finite-rate chemistry, require hypersonic air-breathing engine combustors to be very long – typically a substantial fraction of the length of the vehicle. Accurate computational modeling of the fuel-air mixing process is important for designing combustors. It is therefore critically important for computer codes to accurately predict fuel-air mixing.

Modeling fuel-air mixing using computational fluid dynamics (CFD) requires quantitative flowfield data to evaluate the performance of turbulent mixing models and to develop new models. However, there is a limited database of fuel-air mixing experiments relevant to supersonic combustors in which quantitative or semi-quantitative flowfield measurements have been performed.<sup>1,2,3,4,5,6,7</sup> Even more scarce are fuel-air mixing experiments that are performed in conjunction with supersonic combustion experiments. In this paper, we use an optical measurement technique to quantify the fuel-air mixing process relevant to supersonic combustion of H<sub>2</sub>. This experiment was performed as part of a larger project that included combustion experiments at the same nominal flow conditions. A particularly useful aspect of the current work is that the temperature and mole fraction of all the major species of hydrogen combustion are measured or inferred on an instantaneous basis. This allows determination of correlations between the different

---

<sup>†</sup> Advanced Sensing and Optical Measurement Branch, MS 236.

<sup>\*</sup> National Research Council Postdoctoral Fellow, Hypersonic Airbreathing Propulsion Branch, MS168.

species mole fractions and between the temperature and species mole fractions. These correlations can be used to evaluate elusive parameters in proposed turbulence models.<sup>8</sup>

It is hoped that this data set, together with the corresponding combustion case (which will be published in a future paper) will address the long-standing question of whether combustion enhances or inhibits fuel-air mixing in scramjet engines. The question of the effect of combustion on mixing is a complicated one. In a confined duct flow, heat release has the effect of reducing Mach number and raising pressure, often quite rapidly. Axial pressure gradients accelerate the lower density portions of the flow (hot and H<sub>2</sub>-fuel rich flow) in the axial direction more than the higher density air, thereby creating shear and stimulating mixing. On the other hand, heat release reduces mixing in an unconfined, zero axial pressure gradient planar mixing layer (e.g., Dimotakis<sup>9</sup>).

We have used the dual-pump coherent anti-Stokes Raman spectroscopy (CARS) method.<sup>10,11</sup> to simultaneously measure temperature and the absolute mole fractions of N<sub>2</sub>, O<sub>2</sub>, and H<sub>2</sub>. From these mole fractions, we infer the mole fraction of H<sub>2</sub>O, thereby determining all the major species of hydrogen combustion. Conventional broadband N<sub>2</sub> CARS<sup>12</sup> uses two spectrally-narrow green beams as pump beams and one spectrally-broad red beam as the Stokes beam. The frequency difference between the green and red beams typically corresponds to the vibrational Raman shift of N<sub>2</sub>. The CARS signal is then a faint, spectrally-broad blue beam that contains the N<sub>2</sub> spectrum. This spectrum can be detected and then fit with a theoretical model on a computer to determine the temperature.

The dual-pump CARS technique used here instead uses one yellow and one green pump beam.<sup>10,11</sup> The same broadband red beam is used as in conventional broadband N<sub>2</sub> CARS. The frequency of the yellow pump beam is chosen so that the frequency difference between the yellow and red beams equals a vibrational Raman resonance of O<sub>2</sub>. Thus, the resulting blue CARS spectrum contains both N<sub>2</sub> and O<sub>2</sub> spectra. The relative intensities of these two spectra provide a measure of the relative mole fractions of N<sub>2</sub> and O<sub>2</sub>.

Coincidentally, several pure-rotational Raman transitions of H<sub>2</sub> are present in these spectral regions as well. These spectra are also measured in the present experiment, allowing the relative mole fractions of N<sub>2</sub>, O<sub>2</sub> and H<sub>2</sub> to be quantified simultaneously. By assuming that the only other species present are argon and H<sub>2</sub>O, the absolute mole fractions of the four major species of hydrogen combustion can be determined.

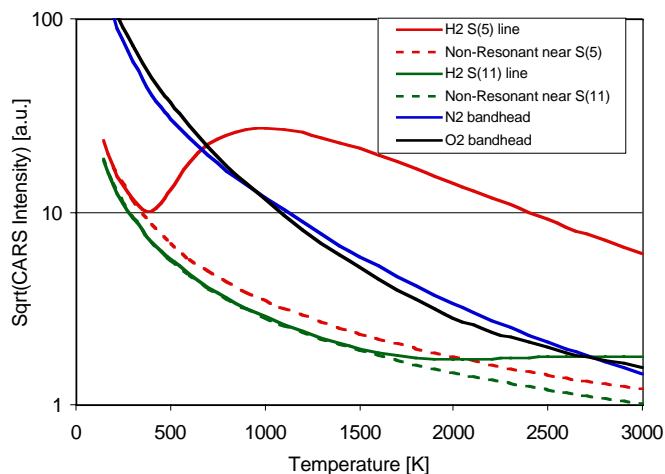


**Figure 1.** Theoretical prediction of the square-root of the peak CARS signal intensity versus temperature, assuming equal mole fractions,  $\chi_i$ , of the four major species of hydrogen combustion ( $\chi_{N_2} = \chi_{O_2} = \chi_{H_2} = \chi_{H_2O} = 0.25$ ). The Sandia CARSFIT code, described below, was used to compute the intensities.

In principle, a conventional broadband N<sub>2</sub> CARS system can be used for fuel-air mixing studies involving N<sub>2</sub> and H<sub>2</sub>. The coincidental collocation of the hydrogen S(11) (where 11 is the rotational quantum number and the notation S refers to the change of +2 in the rotational quantum number) pure rotational line and the nitrogen vibrational Raman resonance near 2300 cm<sup>-1</sup> can be used to infer N<sub>2</sub> / H<sub>2</sub> mixing ratios. However, as Figure 1 shows, below 1500 K the S(11) line has very little signal above the non-resonant background. On the other hand, the spectrum of a dual-pump CARS system probing O<sub>2</sub> and N<sub>2</sub> exhibits a coincidental S(5) hydrogen line. The lower rotational quantum

number results in a much larger population of this transition at moderate temperatures. According to Figure 1, the S(5) line has substantial CARS signal intensity above 400 K. Thus, the dual-pump CARS system is a sensitive probe of  $N_2$ ,  $O_2$  and  $H_2$  over the full range of interest in the present mixing flowfield where temperatures between 350 K and 1500 K are encountered.

### **COMBUSTOR MODEL AND FLOW FACILITY**

The experiment was conducted in NASA Langley's Direct-Connect Supersonic Combustion Test Facility (DCSCTF).<sup>13</sup> The facility is designed to test the combustor of a scramjet engine by directly connecting the facility nozzle exit to the entrance of the combustor. The flow rates are usually selected so that the mass fraction of oxygen is the same as that of standard air. However, in the current experiment, additional nitrogen was supplied instead of oxygen. This resulted in a flowfield with similar enthalpy, pressure, temperature and velocity to the normal operational mode, but with the absence of oxygen. This gas composition inhibits combustion and allows mixing to be directly studied. The high-pressure, vitiated gas is accelerated through a water-cooled convergent-divergent Mach 2 nozzle, before entering the test model.

The test conditions are nominally representative of Mach 7 flight. Gas flow rates to the heater are:  $0.978 \pm 0.019$  kg/s air,  $0.0288 \pm 0.0005$  kg/s hydrogen, and  $0.248 \pm 0.006$  kg/s nitrogen. The heater stagnation pressure is  $0.767 \pm 0.008$  MPa. All uncertainties presented in this paper are based on the 95% probability limits (1.96 times the standard deviation). The above uncertainties are due to the random run-to-run variations and do not include  $\pm 3\%$  uncertainty in the mass flow rate measurements.

Heater and nozzle exit conditions are estimated from the flow rates, heater pressure, and nozzle minimum and exit areas using one-dimensional (1D) analysis detailed in Reference 13. The nominal calculated conditions, and uncertainties due to mass flow rate measurement error and run-to-run variations in heater conditions are: heater stagnation temperature  $1831 \pm 75$  K, exit temperature  $1173 \pm 60$  K, exit pressure  $101 \pm 1.5$  kPa, exit Mach number  $1.994 \pm 0.005$ . Errors arising in the calculation due to the assumption of 1D flow (the effects of non-uniform composition, boundary layers, etc.) are believed to be small. A study of the flow quality at the exit of the facility nozzle was previously conducted<sup>14</sup> and has been summarized in Reference 13.

The test model is shown in Fig. 2; flow direction is from left to right. The model consists of two main sections of duct: a copper section upstream and a carbon steel section downstream. Stainless steel flanges and carbon gaskets separate the sections from each other and the nozzle. Proceeding from left to right, there is a Mach 2 nozzle, a constant area segment, a small outward step at the top wall, a second short constant area segment followed by a constant  $3^\circ$  divergence of the top wall. The span is constant at 87.88 mm. The fuel injector is located just downstream of the start of the  $3^\circ$  divergence. The injection angle is  $30^\circ$  to the opposite wall. The injector nozzle is designed by the method of characteristics to produce Mach 2.5, 1D flow at the injector exit. Hydrogen injection is provided at a stagnation pressure of  $2.12 \pm 0.07$  MPa, a stagnation temperature of  $302 \pm 4$  K. Under normal operation, in which the oxygen is replenished to the freestream gases, this fuel flow rate corresponds to an equivalence ratio of  $0.99 \pm 0.04$ .

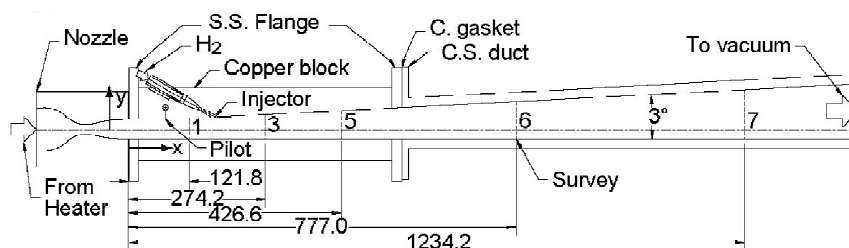


**Figure 2.** Schematic of scramjet combustor model. All dimensions are in millimeters.

The duct is uncooled; however, the wall thickness of the copper duct is greater than 32 mm and the carbon steel duct is 19-mm thick. Thus, given the good thermal conductivity of these materials, it is possible to operate the facility with the model fueled for run times well in excess of 20 seconds, without reaching excessive temperatures. With atmospheric temperature air flowing in the model between runs, runs could be repeated every 10-15 minutes. A total of 15-25 runs could be obtained per day.

The model is equipped with 7 slots to allow the CARS beams to penetrate the duct, of which only slot 5 was used in this study. The slots are in pairs, one on each side of the duct, 4.8 mm wide, extending the full height of the duct. When not in use the slots are plugged flush to the wall. Windows covering the slots are mounted at the end of short rectangular tubes at the Brewster angle, to minimize reflections. The window tubes are ventilated with a constant flow of electrically heated (~400 K) dry air to prevent condensation of water from the heater on the windows. The CARS interaction region can thus be translated the full span and height of the duct without damaging the windows.

The model is instrumented with both pressure taps and wall temperature probes, though only the pressure data is presented in this paper. Thirty-five static pressure taps are located in the copper duct, consisting of 0.80-mm diameter square-edged holes. Taps are located on the bottom wall, at the centerline, and on the top wall at  $z = -36.3$  mm ( $z$  is measured from the horizontal center line). Forty-nine static pressure taps are located in the steel duct, consisting of 1.6 mm diameter square-edged holes. Taps are located at top and bottom wall centerlines, and sidewall midpoints. Pressures are measured with an accuracy of  $\pm 0.6$  kPa by a Pressure Systems Inc. electronically scanned pressure-measuring system.

### **CARS EXPERIMENTAL SYSTEM**

The dual-pump CARS system used an unseeded frequency-doubled Nd:YAG laser (Spectra Physics DCR-4) which produced about 550 mJ per pulse at 532 nm. The pulse duration was about 10 ns and the repetition rate was 10 Hz. The output of the YAG laser was split three ways. Approximately 80 mJ was used as the green pump beam for CARS. A homemade, conventional axially-pumped broadband dye laser operating at 607 nm was pumped by 250 mJ of green light from the YAG. This 607-nm beam was used as the red Stokes beam. The dye solution contained Rhodamine 640 laser dye in methanol. The lineshape of the broadband laser was well represented by a double-Gaussian, the main Gaussian having a width of approximately  $130\text{ cm}^{-1}$ . The double-Gaussian was necessary to ensure proper normalization in the wings of the spectrum, particularly since the spectrum includes strong  $\text{H}_2$  lines in that spectral region. Additional details about the above components of the laser system can be found in reference 13.

From the YAG laser, 200 mJ was used to pump a 554-nm narrowband dye laser (Lambda Physik, FL3002) that had been converted from excimer pumping to YAG pumping. This 554 nm beam was used as the second (yellow) pump beam. The FL3002 dye laser oscillator beam usually reflects twice from the grating before passing to the amplifier. The second reflection is used to reduce the laser's amplified spontaneous emission (ASE). During the process of converting the FL3002 for pumping with a YAG laser, Lambda Physik recommends inserting a mirror into the grating chamber to prevent the second reflection off the grating, reducing the possibility of grating damage. This modification was performed, but caused the level of ASE to increase markedly. The additional ASE generated a low-amplitude, but wide pedestal on the narrowband dye laser spectrum.

The green and red beams were combined using a dichroic mirror. These two beams plus the yellow were then passed through a spherical lens having a focal length of 410 mm. Planar BoxCARS phase-matching geometry was used, with the green and red beams overlapping. The probing volume formed at the intersection of the three beams had a minimum diameter of  $130\text{ }\mu\text{m}$  (FWHM), measured by traversing a knife edge across the foci of all three beams. The probe volume is 1.8 mm long (FWHM), as measured by traversing the probe volume across a thin planar jet of nitrogen gas, surrounded by a 30-mm-diameter jet of argon, and measuring the  $\text{N}_2$  CARS signal as the probing volume was traversed across the nitrogen sheet.

A second 410-mm focal-length lens collected and collimated the three input beams as well as the blue CARS signal beam at 491 nm. Two dichroic mirrors that efficiently reflected blue while transmitting yellow light were arranged in a multi-reflection configuration to isolate the blue signal beam. This blue beam was then directed into a one-meter spectrometer (McPherson) with a 1200 groove/mm grating. Two cylindrical lenses provided a sharp horizontal focus at the spectrometer entrance that was reimaged, spectrally dispersed, at the detector. The detector was a 1100x330-pixel, non-intensified, back-illuminated, CCD camera (Pixel Vision, SV11CBJ). A LabView interface downloaded the spectra to a PC for subsequent analysis and to display the data in real-time for signal optimization. The 330-pixel region was binned into three separate rows of 110 pixels before read-out to allow more rapid acquisition of data. This resulted in three 1100-pixel spectra per laser pulse, with a spectral resolution of  $0.74\text{ cm}^{-1}$ .

per pixel. The CARS signal was imaged onto the first two of these regions, with the contributions of dark noise and laser scatter acquired on the third bin region. Distributing the signal over two bin regions increased the dynamic range of the measurements by a factor of two. The binned background was subtracted from each of the signal bin regions before the signal regions were summed to form the total spectrum.

The spectral non-uniformity of the Stokes laser was accounted for by normalizing the CARS signal to an averaged non-resonant CARS signal obtained immediately after completion of the day's runs. The profile of the broadband laser was measured by obtaining nonresonant CARS spectra in a flow of argon, averaged over 200 laser pulses. A sum of two Gaussian functions was fitted to the broadband laser profile, as mentioned above. Each of the image acquisitions was normalized using this fitted profile.

Recently, this same CARS system was characterized by making measurements in an atmospheric-pressure furnace and a laminar flat-flame burner.<sup>15</sup> Average values and root-mean-square (RMS) deviations were determined. Mean temperature measurements in a furnace containing air between 300 and 1800 K agreed with thermocouple measurements within 26 K on average, while mean mole fractions agreed to within 1.6 % of the expected value. The temperature measurement standard deviation averaged 64 K while the standard deviation of the species mole fractions averaged 7.8% for O<sub>2</sub> and 3.8% of the measured value for N<sub>2</sub>, based on 200 single-shot measurements. Measurements were performed in a hydrogen-air laminar flat-flame Hencken burner for fuel-lean and fuel-rich conditions. For fuel-lean conditions, good agreement was found for temperature between the data and an adiabatic, equilibrium computation. Temperatures measured under fuel-rich conditions were about 50 K higher than the computation. Mole-fractions for N<sub>2</sub> agreed with the computation to within 3%. Measured O<sub>2</sub> mole fractions were systematically high by 0.01 to 0.02 while measured H<sub>2</sub> mole fractions were systematically low by 10-15% compared to the computation. For an equivalence ratio of 2.8, the standard deviation of 58 single-shot temperature measurements was 108 K, or 5.8%, and the standard deviations of H<sub>2</sub> and N<sub>2</sub> mole fractions were 9.8% and 3.8% of the measured values, respectively. Though the data analysis method has been improved since these data were analyzed, these values are indicative of the measurement precision in the current experiment. They do not account for the generally lower signal-to-noise ratio experienced in a large-scale facility when compared with more easily-controlled small-scale flame experiments.

### **CARS SPECTRAL DATA ANALYSIS**

Throughout the day's facility runs the center frequency of the broadband dye laser spectrum varied by 30 cm<sup>-1</sup> or more due to variations in laser alignment and dye temperature, although the shape of the spectrum was nearly constant. A shifted dye laser spectrum manifested itself as a gradient in the baseline signal of the data spectrum. The fitting routine accounted for an offset in the non-resonant spectrum by fitting the middle one-third of the acquisitions three times, using values of non-resonant shift that differed by 7.4 cm<sup>-1</sup>. The total residual for the best fits to these spectra was computed for the three shifts, and additional calculations performed if necessary until a minimum residual was found. A parabola was then fitted to the three points having the lowest residual, and the minimum of the parabola was taken to be the correct non-resonant shift. This method determined the shift in the non-resonant to within 3.5 cm<sup>-1</sup>, or 2.7% of the Stokes laser's Full Width at Half Maximum (FWHM).

Another experimental factor that must be accounted for is the instrument function of the detection system used to image the CARS signal. The signal beam was focused at the spectrometer entrance with the slit wide open, to avoid aperturing or blocking of the CARS signal caused by beam steering. The focus of the CARS signal on the entrance slit of the spectrometer could change both width and position from one set of measurements to the next. An iterative technique was used to determine the width of this instrument function. The function was assumed to be the sum of two Gaussian functions, a narrow distribution and a wider distribution of lower amplitude forming a "pedestal" for the main portion of the instrument function. The widths and relative amplitudes of the distribution were determined for a given day's runs by fitting with a nominal (initial guess) instrument function and a tunnel spectrum containing a hydrogen rotational line. The hydrogen line was chosen because it is narrow compared to the instrument response.

During determination of the instrument function, the CARSFIT code,<sup>16</sup> developed at Sandia National Laboratories, Livermore, CA, was used to fit for temperature and mole fractions. The initial guess instrument function was first used to best fit the experimental spectrum. This provided a first estimate of the flow conditions and

produced an unconvolved theoretical spectrum. The instrument function parameters were then fitted by convolving this theoretical distribution with the two laser profiles and the detector instrument function until a best fit to the tunnel data was obtained. A Levenberg-Marquardt nonlinear least-squares fit routine, part of the MINPACK library<sup>17</sup>, was used to determine the parameters of the instrument function. This instrument function was then used to fit the conditions with CARSFIT and the procedure repeated until the instrument function and the fitted conditions changed by less than 5%. In general, the FWHM of the main Gaussian portion of the instrument function was between 1.2 and 2.1  $\text{cm}^{-1}$ , with the secondary Gaussian about 24  $\text{cm}^{-1}$  FWHM and 5% of the amplitude of the main Gaussian. A single instrument function was used to analyze a given day's runs.

In our previous work we used CARSFIT to produce a library of spectra for various values of temperature and  $\text{N}_2$  concentration.<sup>13</sup> However, the current application of dual-pump CARS is significantly more challenging, owing to the additional fit parameters of  $\text{O}_2$  and  $\text{H}_2$  mole fractions. The presence of  $\text{H}_2$ , in particular, complicates the analysis because hydrogen spectral lines are rather narrow, causing the spectral code to increase the number of spectral computation points dramatically (by over an order of magnitude). In addition to slowing the computation, this also makes the required 4-dimensional (temperature,  $\text{N}_2$ ,  $\text{O}_2$ , and  $\text{H}_2$  mole fractions) quick-fitting libraries extremely large, requiring 80 MB for a database of 29 temperature values and 10 mole fraction values for each of the three measured species. Still, using libraries of CARSFIT spectra to fit the data is preferable to other possible methods such as using CARSFIT's internal fitting algorithm. The size of the library was kept to a minimum by making the temperature and mole fraction increments relatively large and then using interpolation to more precisely determine the best-fit parameters. The next several paragraphs describe in more detail why and how these libraries are created and how they are used to fit the data.

One of the more challenging aspects of multi-parameter CARS measurements involves determining best-fit values of the measurement parameters in a robust and repeatable manner. The fitting routine used by the CARSFIT code can fit consistently for temperature and a single mole fraction, but as the number of fit parameters increases, the code experiences more difficulty converging to a least-squares minimum, instead returning the initial conditions or a local minimum. This effect was noted for the dual-pump CARS analysis in Reference 18. The difficulty of achieving converged fit spectra is especially apparent if the starting values for the fit are not close to the converged values. The fitting success tends to be poor when starting from a constant initial guess for the fit parameters and there is a large variation in the flow conditions from one spectrum to the next, as is the case for turbulent mixing or combustor flows.

The fitting problems have been circumvented in this analysis by fitting temperature and mole fractions to a database of spectra previously computed using the CARSFIT code. These calculations are performed using the instrument function for the day of the experiment. The CARSFIT calculation uses a Voigt profile to model the individual Raman transition strengths. The original CARSFIT code was modified to include convolutions with both pump beams and the instrument function<sup>15</sup> as the original version<sup>11</sup> assumed a monochromatic pump beam. The Nd:YAG laser used in these experiments was not injection-seeded, so the laser linewidth is large compared to the linewidth of the individual Raman transitions.

The database contains temperature intervals of 200 K and between 10 and 12 mole fraction values, depending upon the species. Oxygen mole fractions are between 0 and 0.4, while the nitrogen and hydrogen mole fractions vary between 0 and 1. Mole fraction values are more closely spaced near zero, in order to achieve better resolution at low molar concentrations. Each database took 60 hours to generate on a 2.4-GHz DEC alpha processor, and a different database was required for each day's runs, because the instrument function changed day to day.

Initial estimates for temperature and mole fractions were obtained by comparing the area-normalized experimental spectrum to each of the area-normalized theoretical spectra in the database, with the fitted parameters corresponding to the database entry having the smallest least-squares difference to the experimental spectrum. These parameter values were then used as initial conditions for a least-squares fit for the parameters, again using the Levenberg-Marquardt technique. Spectra with fit parameters between the sample values in the database were obtained by linear interpolation from the 16 database points surrounding the interpolation point in the four-dimensional parameter space. If the fitting algorithm requested a point outside the database, estimates were obtained by linear extrapolation from the closest points in the database. Using this technique, it is possible to fit mole fractions below zero by fitting to noise in the data. At first glance, this appears to be unphysical, but over a large

number of measurements, the fitted value should average to zero if the true concentration is zero. Each Levenberg-Marquardt fit was started from the best library-entry temperature fit and the two nearest database temperature entries. Of these three fits, the one with the lowest residual was chosen as the best fit. This technique has the advantage of being very fast relative to fitting with CARSFIT when a large number of spectra need to be fitted, as the spectra in the library only need to be generated once. After the database has been generated, the fitting of 100 spectra requires one minute of computer time. A plane of CARS measurements, consisting of about 3000 spectra, can be fitted for temperature and three mole fractions in about two hours.

A series of numerical tests was performed to assess the interpolation algorithm and to determine the best temperature intervals to use in the fit library. Libraries having 100 K, 200 K, and 400 K temperature increments (but identical mole fraction increments) were computed. These were used to fit 13 theoretically generated spectra spanning the range of temperatures and concentrations expected in the current experiment. Compared to the experimental measurement uncertainty, there was not a significant difference in temperature measurement accuracy between the three libraries. This suggests that linear interpolation is appropriate as presently applied, though CARS has a nonlinear dependence on temperature. The 200K-increment library had the lowest average temperature error (2.1 Kelvin) and lowest average mole fraction error (0.00122 for O<sub>2</sub>, 0.0033 for N<sub>2</sub> and 0.0034 for H<sub>2</sub>). For the 200 K increment library, the worst fit of the 13 trials differed from the known value by 20 K. With the exception of low temperature regions (<400 K) where sensitivity to H<sub>2</sub> is poor, the worst agreement for all mole fractions was 0.008. These errors are significantly lower than the temperature and mole fraction uncertainties for this measurement system determined in the laminar flat flame studies mentioned previously.<sup>15</sup> The signal-to-noise ratios of the measurements in the facility are lower than for the laminar flame, so the uncertainty due to the fitting routine is considered to be small.

The H<sub>2</sub>O mole fraction is not directly measured but it can be inferred from the measured absolute mole fractions of N<sub>2</sub>, O<sub>2</sub>, and H<sub>2</sub>. This inference relies upon a few assumptions. First of all, we assume that Argon gas is present in fixed proportions to the air initially combusted in the heater and to the air that enters the duct from the side window mounts. Furthermore, we neglect the presence of other minor species such as OH. This second assumption could be inappropriate in many combustion situations, particularly at temperatures above 2500 K where minor species can amount to 2% or more, according to our computations using an equilibrium chemistry code. However, in the present work, combustion has been inhibited and the temperature is low (<1300 K), so this assumption is valid. Under these conditions, the following equations may be used to infer the mole fractions of Ar and H<sub>2</sub>O from the measured quantities:

$$\chi_{Ar} = \frac{\chi_{O_2}}{\chi_{O_2,air}} \chi_{Ar,air} + \left( \chi_{N_2} - \frac{\chi_{O_2}}{\chi_{O_2,air}} \chi_{N_2,air} \right) \chi_{Ar,fs} \quad (1)$$

$$\chi_{H_2O} = 1 - \chi_{N_2} - \chi_{O_2} - \chi_{H_2} - \chi_{Ar} \quad (2)$$

where the subscripts *air* and *fs* refer to conditions in standard atmospheric air and to the calculated nozzle-exit mole fractions respectively.

## **MDOE AND RESPONSE SURFACES METHODS**

The experimental data were obtained using a formal experiment design method, known as Modern Design of Experiments (MDOE). This method is detailed in References 19 and 20 and briefly summarized here. The CARS probe volume was scanned through the flowfield along horizontal and vertical lines – one scanned line per tunnel run. The order and direction of these scans was randomized to defend against systematic errors. Repeat measurements were obtained to improve measurement uncertainty and to provide a qualitative determination of the uncertainty and repeatability of the measurement system and flow facility.

After the CARS spectra were processed to determine the temperature and the mole fractions at various locations in the duct, response surfaces were fit to these data to provide quantitative maps of the flowfield parameters.<sup>19,20</sup> In all cases except one, the *cosine series bivariate order 6* function was used to fit the temperature and mole fraction

data as well as the correlations. The O<sub>2</sub> mole fraction data was better fit by *Fourier series bivariate Order 2x3* and this function was therefore used for that data only. These fits provide estimates of the distribution of mean of the measured parameters over the flowfield, since these functions, by virtue of their limited number of fit coefficients (much less than the number of data points), smooth (or average) the data. Using these fitted surfaces to determine mean values of the flowfield parameters one can then compute statistics of the fluctuations in the measured parameters.<sup>13,20</sup> The difference between each measured sample and the mean, denoted by a primed quantity such as  $T'$  for temperature fluctuations and  $\chi_i'$  for fluctuations of species  $i$ , and the chosen fluctuation product, such as  $T'T'$  is found. The fluctuation product data are then fit to a response surface, as described above, to provide an estimation of the distribution of mean values of the product. In this way, the temperature fluctuation autocorrelation,  $\langle T'T' \rangle$ , which is related to RMS temperature fluctuations,  $(\langle T'T' \rangle)^{1/2}$ , can be computed. Similarly, correlations between various fluctuating properties in the flow, such as  $\langle T'\chi_{H_2}' \rangle$  are also calculable.

## **NUMERICAL MODEL**

The numerical results presented in this paper are part of an ongoing effort aimed at applying existing computational fluid dynamics (CFD) models to the SCHOLAR scramjet combustor. A more detailed description of these ongoing calculations may be found in reference 21. Only a brief description will be presented here.

The simulation was done using the VULCAN CFD code developed at NASA Langley.<sup>22</sup> The half-width combustor was discretized with a grid that had approximately 3.6 million control volumes (CVs), uniformly distributed among 80 blocks to take advantage of VULCAN's Message Passing Interface (MPI) capability. Non-C(0) block-boundaries were extensively used to reduce grid density requirements. The vertical grid dimensions varied between 61 and 85, and the lateral between 61 and 81. The grid spacing at the wall varied between  $1.5 \times 10^{-4}$  m and  $3.0 \times 10^{-4}$  m. For the most part, the resulting values of wall units,  $y^+$ , are below 100, which is appropriate for the use of wall functions.

The gas was modeled as a mixture of thermally-perfect gases comprising N<sub>2</sub>, H<sub>2</sub>O, and H<sub>2</sub>. The inflow was obtained from a numerical simulation of the facility nozzle, with mass-fractions 0.794 and 0.206 for the N<sub>2</sub> and H<sub>2</sub>O species, respectively. The small contribution of argon (<1%) was neglected. The inflow conditions at the inlet of the hydrogen injector were assumed to be subsonic with total pressure and temperature of 3.44 MPa and 302 K, respectively. These conditions resulted in an equivalence ratio of approximately 1.0. The solid walls were modeled as no-slip isothermal, with wall temperatures set at 400 K and 500 K for the copper and steel sections, respectively. The exit boundary was modeled as supersonic extrapolation, and the vertical centerplane was modeled as a symmetry boundary.

The inviscid fluxes were calculated using Edwards' low-dissipation flux-split scheme,<sup>23</sup> with third-order MUSCL interpolation. Time-integration was done using the implicit diagonalized approximate-factorization scheme<sup>24</sup>; the entire domain was run fully elliptic. The Wilcox k- $\omega$  turbulence model and wall functions were used.<sup>25</sup> They were supplemented with the Wilcox compressibility correction, used to reduce spreading rates (or turbulence) as a function of the local turbulence Mach number.<sup>25</sup> Not included was the Pope correction for the round-jet/plane-jet anomaly, which is standard in Wilcox's model. The turbulence Prandtl ( $Pr_T$ ) and Schmidt ( $Sc_T$ ) numbers were set at 1.0.

A three-level grid sequencing was used for convergence acceleration and to estimate grid convergence. Computations were done on 16 DEC Alpha 667 MHz nodes in a BEOWULF cluster. The computations took approximately 4 days to run.

## **CARS RESULTS**

### **Single-Shot CARS Spectra**

This section shows several single shot CARS spectra that are representative of the data obtained in the experiment. These spectra help illustrate some of the benefits of using the dual-pump CARS method, such as the good signal-to-noise ratio obtained. They also help to illustrate some problems that occurred during the analysis.



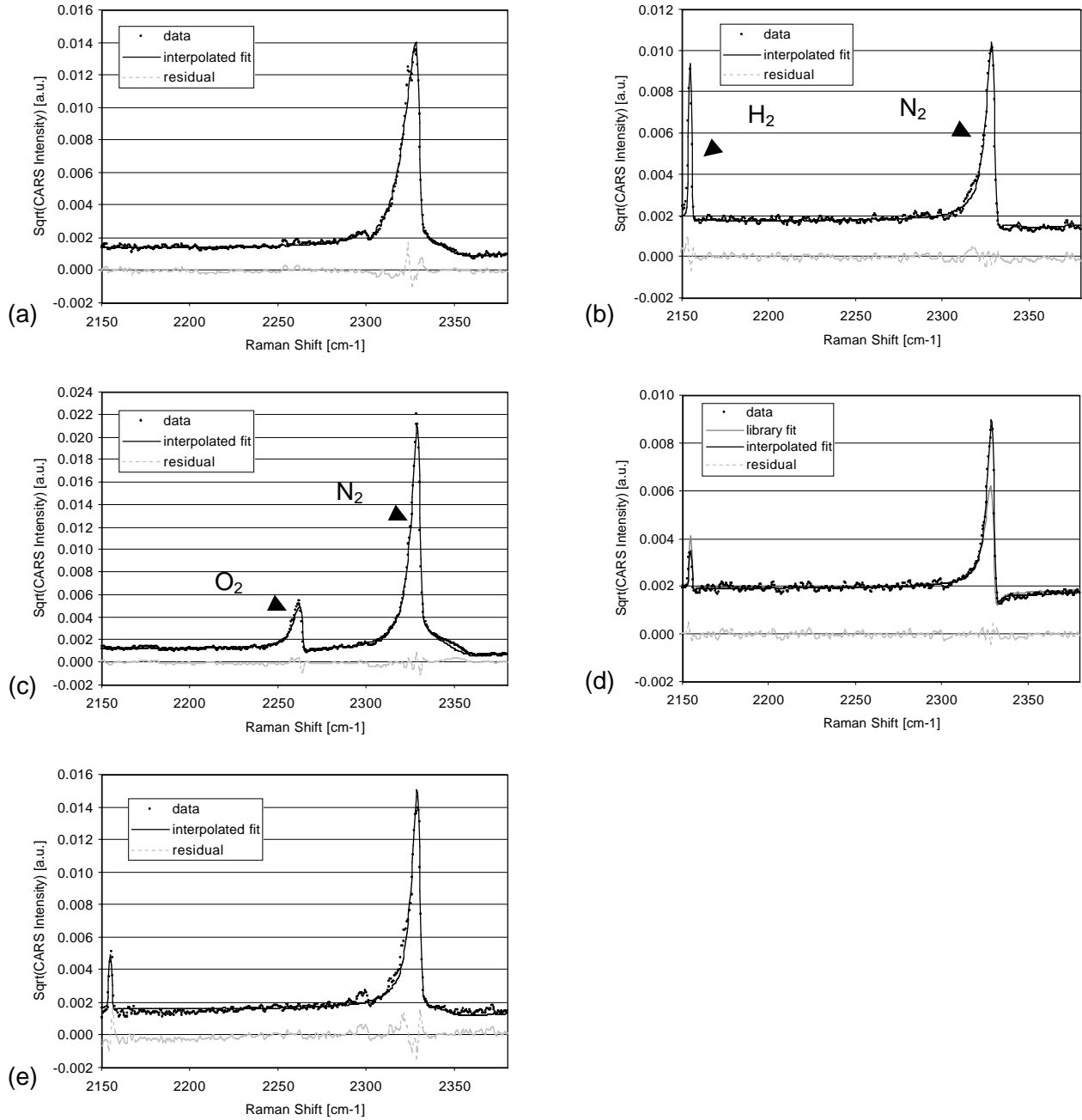


**Figure 3.** Single-shot spectra obtained in the combustor. These five spectra show different flow conditions, as described in the text.

Figure 3(a) shows a typical spectrum that is characteristic of the unperturbed freestream gas: gas that is far from the fuel jet and far from the CARS beam windows. It shows a high mole fraction of relatively warm  $N_2$  and negligible mole fractions of  $O_2$  and  $H_2$ . Such spectra were found in an annular ring outside of the fuel jet and at the top and bottom walls of the tunnel.

Closer to the center of the duct, many of the spectra resembled Figure 3(b). This spectrum shows relatively cooler gas containing both  $N_2$  and  $H_2$ , but no  $O_2$ . The gas at the center of the duct tended to be cooler than the periphery because the  $H_2$  is very cold ( $\sim 133$  K) when injected.

Spectra that resemble relatively cool air were measured near the side walls of the tunnel, as shown in Figure 3(c). Since almost no  $O_2$  passed through the tunnel nozzle, it is likely that this gas was either inside the window cavities or was being drawn into the duct from the air-based window purging system attached on the windows on both sides of the duct. This point is discussed further below.

Figure 3(d) demonstrates the ability of the interpolation algorithm to fit the experimental data precisely. Two theoretical fits to the data are shown. The fit corresponding to the closest library entry is shown. Also, the interpolated fit is shown. Clearly, the interpolated value produces a much more accurate fit. Had interpolation not been used, large errors in the data would have been introduced.

A problem that occasionally (<1% of the time) occurred when analyzing the CARS spectra was that some spectral shapes did not correspond to those generated by CARSFIT. Figure 3(e) shows a spectrum in which the ground vibrational band of nitrogen is well fit, but the excited vibrational band is not. This spectrum is characteristic of a ‘two temperature’ CARS spectrum that occurs when the CARS probe volume samples a volume that contains both hot and cold gas. Our analysis method does not account for this situation, though other researchers have determined schemes for fitting this type of spectrum.<sup>26</sup> Luckily, this problem is rarely found in the current data set, so bias errors associated with this problem are expected to be small.

An interesting artifact of the present fitting algorithm is that negative mole fractions are sometimes obtained. For example, some spectra, due to random noise, exhibit a small dip in the CARS signal near one of the  $H_2$  lines. This dip results in a negative mole fraction of hydrogen. While this is obviously unphysical, allowing negative mole fractions due to noise is important to avoid the introduction of bias errors in the measurement of the mean mole fraction, as mentioned above.

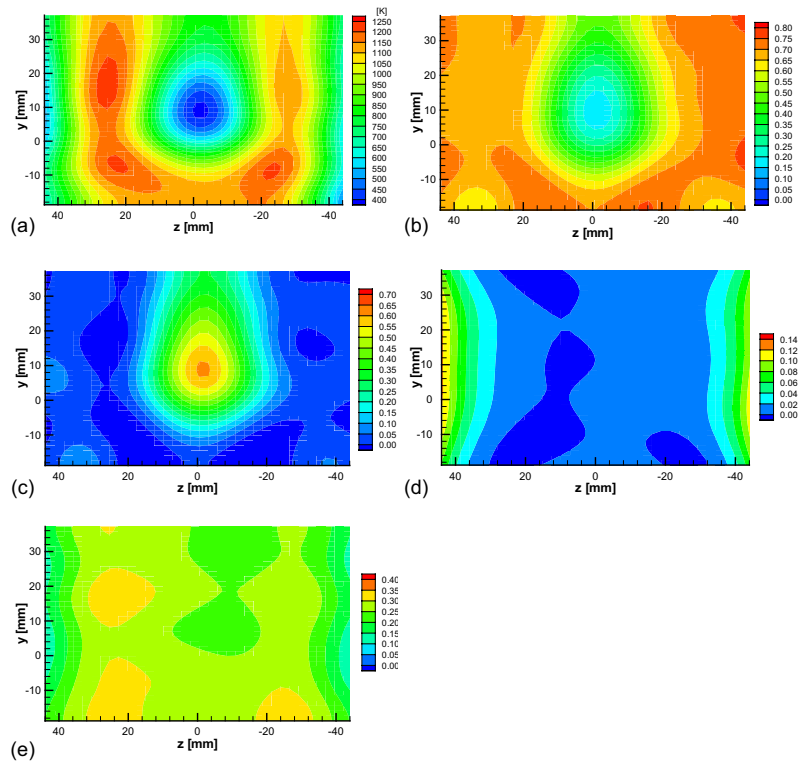


**Figure 4.** Maps of various flow parameters in plane 5: (a) temperature, (b)  $\chi_{N_2}$ , (c)  $\chi_{H_2}$ , (d)  $\chi_{O_2}$ , and (e)  $\chi_{H_2O}$ .

### Mean Property Maps

The mean temperature field and the mean species maps, measured by the CARS system and fit with response surfaces, are shown in Figure 4. The temperature map in Figure 4(a) shows a circular cold region at the center of the duct. Inspection of the mean  $H_2$  field in Figure 4(c) indicates that this low-temperature region is associated with the

remnants of the cold  $H_2$  fuel jet injected upstream. In fact, the hydrogen was injected at 133 K, far below the freestream temperature at the nozzle exit, predicted to be  $1173 \pm 60$  K. Surrounding the fuel jet is a region of relatively warm gas at approximately 1100–1200 K, with slightly higher temperatures on the left side of the image. This region of the flowfield is mostly  $N_2$  and  $H_2O$ : the unperturbed freestream gas. The  $H_2$  mole fractions vary from zero near the edges of the duct to 0.61 near the duct center.

On the left and right sides of the duct the temperature decreases significantly. Inspection of the  $O_2$  mole fraction map in Figure 4(d) indicates the presence of more than 10% of  $O_2$  in these regions. We believe that this decrease in temperature and increase in  $O_2$  mole fraction is caused by the warm dry air blown over the CARS beam input windows to prevent condensation of water. This air is present in the window space and also is entrained into the duct. The ability to measure  $O_2$  mole fraction allows us to determine the extent of the influence of the air pumped into the cavity on the mixing flowfield. This is also useful as an indicator of this extent for combustion tests, where there is no way of telling the externally introduced air from freestream air cooled by the duct wall.

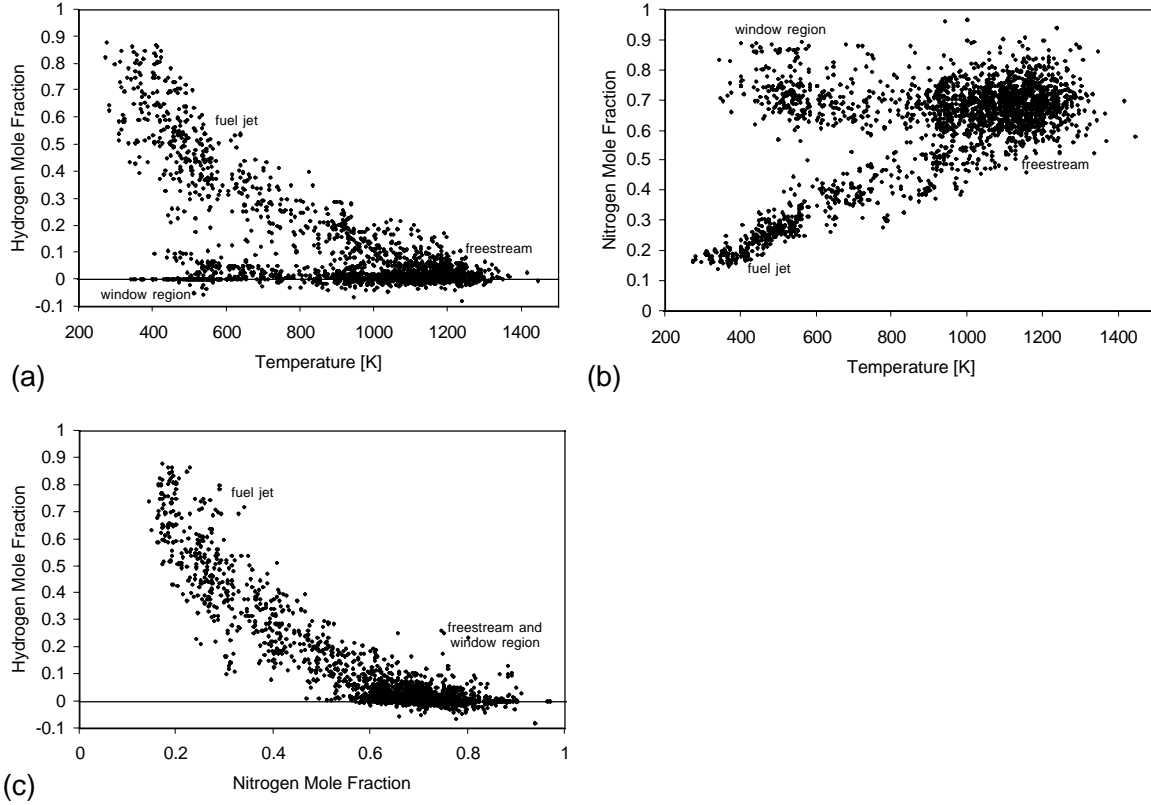
The  $N_2$  mole fraction map, shown in Figure 4(b) shows a relatively uniform, high mole fraction ( $\sim 0.70$ ) of nitrogen around the periphery of the jet. This mole fraction is not unity because approximately 30% of the freestream is water generated during the vitiation process. The measured freestream  $N_2$  mole fraction agrees well with the freestream conditions predicted by the 1D calculation. The measured mole fraction of  $N_2$  at the center of the fuel jet is about 0.17.

Figure 4(e) shows the  $H_2O$  mole fraction map inferred from Figures 4(b)-(d) and using Equations (1) and (2). As expected, the mole fraction of  $H_2O$  is about 0.3 away from the fuel jet and away from the tunnel windows. One unexpected result is that the  $H_2O$  mole fraction is approximately constant across the image, dipping only slightly near the fuel jet. The  $H_2O$  mole fraction was expected to closely track the  $N_2$  mole fraction, which varies significantly over the flowfield. It is presently unclear whether this unexpected behavior is real or is part of a systematic error in the method used to infer the water mole fraction. It is plausible that water could be diffusing into the jet faster than nitrogen. However, this anomaly is much more likely to be caused by errors in fitting for the concentrations of the other species, particularly hydrogen. Previously, we showed that our method underestimated the  $H_2$  mole fraction by 10-15% in fuel-rich conditions of a hydrogen flame. This caused water mole fractions (inferred by difference) to be artificially elevated by the same amount. The same error could be present in the current experiment, which would explain the anomaly. Clearly, a direct measurement of the  $H_2O$  mole fraction would be preferred to inferring it.

Parameter	Statistical Uncertainty of Fit 95% CIHW	Absolute Maximum Value of Fit	Statistical Uncertainty of fit in % 95% CIHW
T	38	1230	3.1
$\chi_{N_2}$	0.022	0.768	2.8
$\chi_{H_2}$	0.024	0.612	4.0
$\chi_{O_2}$	0.005	0.202	2.6
$\chi_{H_2O}$	0.019	0.329	5.8
$T'T'$	16672	96390	17.3
$\chi_{N_2}'\chi_{N_2}'$	0.006	0.024	25.1
$\chi_{H_2}'\chi_{H_2}'$	0.011	0.055	19.9
$T'\chi_{N_2}'$	9.5	39.2	24.3
$T'\chi_{H_2}'$	12.1	48.0	25.2
$\chi_{N_2}'\chi_{H_2}'$	0.007	0.025	27.8

**Table 1.** Uncertainty in fitted surfaces, determined using response surface methodology. The first five entries show uncertainties resulting from fits to the entire data plane, as shown in Figure 4. The other entries show uncertainties from surface fits to the cropped data plane, as shown in Figure 6. Temperature is in Kelvin and mole fractions are unitless.

Table 1 summarizes the uncertainty in the fits in these mean quantities. These values represent the 95% Confidence Interval Half Width ( $CIHW_{95\%}$ ) uncertainty in the fit's prediction of the mean surface, averaged of the entire surface. However, since the flow is has substantially steeper gradients and more fluctuations near the fuel plume, the uncertainty in that region is larger than average whereas the uncertainty in the more stable regions of the flow are smaller than average.



**Figure 5.** Correlation graphs comparing (a)  $T$ - $\chi_{H_2}$  correlation, (b)  $T$ - $\chi_{N_2}$  correlation, and (c)  $\chi_{N_2}$ - $\chi_{H_2}$  correlation.

### Correlations in Measured Quantities

Since the temperature and mole fraction data were obtained simultaneously, we can measure correlations between the different measured parameters. While five parameters have been measured or inferred, those of primary interest in the present experiment are temperature and the mole fractions of  $N_2$  and  $H_2$ . Molecular oxygen is only present at the edges of the flowfield, and does not participate in the mixing of the injected fuel. Water, presumably, should primarily track with the  $N_2$  gas in the bulk of the flowfield. Thus, three correlations of interest are those between  $T$  and  $\chi_{H_2}$ , shown as a scatter plot in Figure 5(a),  $T$  and  $\chi_{N_2}$  in Figure 5(b), and  $\chi_{H_2}$  and  $\chi_{N_2}$  in Figure 5(c). Each of these graphs shows three distinct regions of the flow: the partially-mixed fuel plume (ie. the mixing layer), the unperturbed freestream and the gas near the windows. In Figure 5(a), note that in the mixing layer, there appears to be a linear relationship between  $T$  and  $\chi_{H_2}$ . As expected, the higher mole fractions of  $H_2$  tend to be colder, with the opposite trend being true for  $N_2$ .

### Spatial Variation of Correlations in Fluctuating Parameters

When  $\langle T'T' \rangle$ ,  $\langle T'\chi_{H_2}' \rangle$  and other correlations were computed using the same data set, a significant problem occurred: the shape of the surface fits became very sensitive to the order of the fitting functions. For example, 5<sup>th</sup>, 6<sup>th</sup> and 7<sup>th</sup> orders of the cosine series bivariate functions produced very different looking maps of  $\langle T'T' \rangle$  while 8<sup>th</sup>, 9<sup>th</sup>, and 10<sup>th</sup> orders were more qualitatively similar. Typically, in a good surface fit to the data, the shape of the surface is

nearly independent of the fit order. This observation indicated that a 6<sup>th</sup>-order fit did not contain enough curvature to capture the variations in the data. However, it is undesirable to use higher orders because the number of fit parameters increases substantially, which increases the uncertainty in the fit and also introduces high-frequency artifacts into the fit surface. Two modifications were made to the data to allow good fits to be obtained. First, the data near the side windows ( $z < -30$  mm and  $z > 30$  mm) was cropped to remove the steep temperature and mole fraction gradients there. The data in this region were not considered particularly useful anyway since injection of cooling air from the window slots was not modeled by the CFD. Second, we assumed spanwise symmetry about the center of the fuel jet. This second assumption is thought to be fair (i.e., the errors introduced are significantly less than the extra errors inherent in the fitting if the assumption is not made) in the present flowfield, especially considering that the results are to be compared with symmetric CFD. Making these assumptions effectively halves the grid spacing of the measurements, thereby sampling the shape of the fuel jet more precisely. The plane of symmetry was determined from the data and not assumed to be the plane of symmetry of the duct.

As described in References 19 and 20, several statistical tests are applied to the data to ensure that the surface fit model provides a good representation of the data. The mean quantity maps shown in Figure 4 passed the required statistical tests, particularly the *Model F-Statistic* test, the *Lack-of-fit F-Statistic* test and the *Lack of Fit P-Statistic* test. The maps shown in Figure 6 all pass the *Model F-Statistic* test, indicating that there is sufficient signal-to-noise in the data to allow a good fit. However, these maps obtain values of 1.2-1.4 for the *Lack-of-fit F-Statistic* test, whereas this parameter should ideally approach unity if the surface fits the data well. Similarly, the *Lack of Fit P-Statistic* test resulted in values less than 0.001 in each case, whereas this parameter should be greater than 0.05 if the model is a good fit to the data. In our previous work, where we encountered the same problem, we found that by breaking the surface up into smaller spatial regions, we could satisfy these criteria, though at substantial effort. However, Box and Draper<sup>27</sup> comment on this very topic in their classic text on response surface methods: "Occasionally, and particularly when there is a very large amount of data, investigation might show that the deficient model is, nevertheless, sufficient for the purpose at hand and therefore may be used with proper caution." In the present paper, we acknowledge that the computed surfaces in Figure 6 and Figure 8 do not precisely fit the data, and therefore should be used with caution.

Figures 6(a)-(f) show maps of  $\langle T'T' \rangle$ ,  $\langle \chi_{H_2}' \chi_{H_2}' \rangle$ ,  $\langle \chi_{N_2}' \chi_{N_2}' \rangle$ ,  $\langle T' \chi_{H_2}' \rangle$ ,  $\langle T' \chi_{N_2}' \rangle$ , and  $\langle \chi_{H_2}' \chi_{N_2}' \rangle$  in the duct. Several observations can be drawn. First, all of the figures show an annular ring around the fuel jet, indicating that maximum fluctuations occur near the edges of the fuel jet, by comparison with the mean  $H_2$  map in Figure 4(c). This result is observed from all six maps even though the parameters measured and computed are, for the most part, wholly independent of each other. Second, it is clear that the intensity of these fluctuations is greater near the bottom of the duct, where it is expected that the shear would be greatest. Note that for each quantity, the center of the fuel plume has relatively lower levels of fluctuation than the edges of the jet. Figure 6(d) shows another interesting feature: the edge of the fuel plume reaches values of  $\langle T' \chi_{H_2}' \rangle$  approximately equal to -65 K compared to approximately zero far from the jet. The significance of this number is that near the edge of the fuel jet, large negative fluctuations in temperature correlate with large positive fluctuations in  $H_2$  mole fraction and vice versa, because the injected  $H_2$  is cold. As expected, Figure 6(e) shows almost exactly the opposite affect: the edge of the fuel jet reaches values of  $\langle T' \chi_{N_2}' \rangle$  approximately equal to +65 K for the same reason. The map of  $\langle \chi_{H_2}' \chi_{N_2}' \rangle$  shown in Figure 6(f) tends from approximately zero away from the jet to -0.04 at the edge of the fuel jet. This shows that  $N_2$  and  $H_2$  are anti-correlated in this shear layer: when the mole fraction of  $N_2$  is higher than average, the mole fraction of  $H_2$  is lower than average, and vice versa – this is obviously qualitatively correct. In addition to adding to our intuitive understanding of the fuel-air mixing process, correlation maps such as these could be used to develop turbulence models for CFD codes.

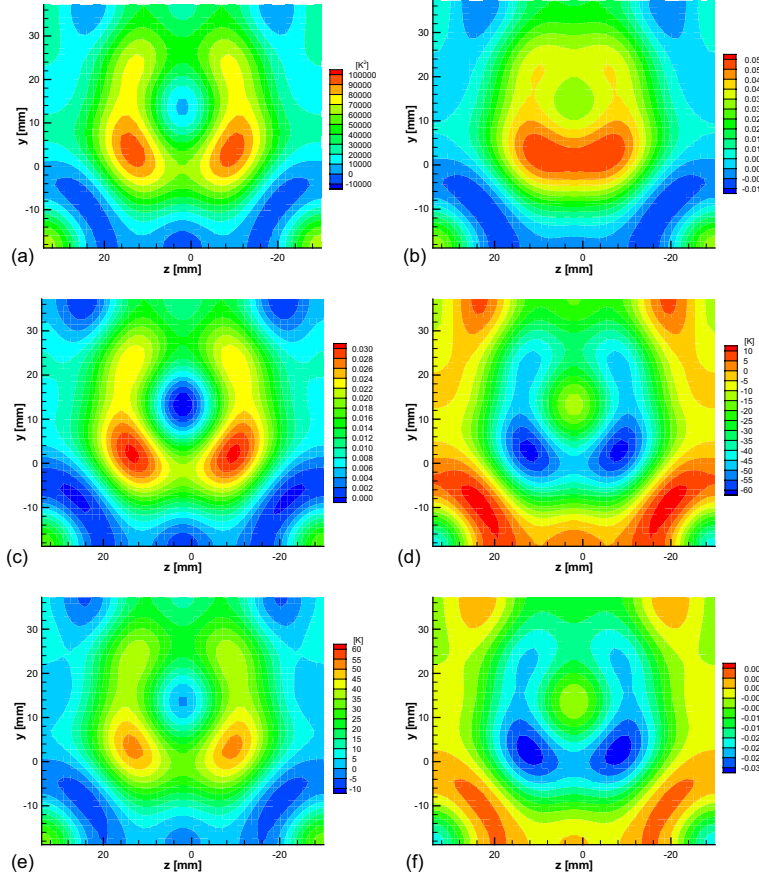


**Figure 6.** Maps of correlations between fluctuating quantities: (a)  $\langle T'T' \rangle$ , (b)  $\langle \chi_{H2}'\chi_{H2}' \rangle$ , (c)  $\langle \chi_{N2}'\chi_{N2}' \rangle$ , (d)  $\langle T'\chi_{H2}' \rangle$ , (e)  $\langle T'\chi_{N2}' \rangle$ , and (f)  $\langle \chi_{H2}'\chi_{N2}' \rangle$ .

Table 1 summarizes the uncertainties in these fluctuating quantities. However, caution must be applied when interpreting these numbers for two reasons. First, these estimates assume that the model is a good fit to the data, which isn't precisely true in this data set because the models failed the *Lack-of-Fit F-statistic* and *P-statistic* tests. Second, these uncertainties are averaged over the whole surface. The uncertainty in regions near the fuel plume are larger than average whereas the uncertainty in the more stable regions of the flow are smaller than average.

## COMPARISON BETWEEN CARS AND CFD

### Mean Property Maps

Figure 7 shows a comparison between mean temperature and species mole fraction maps and the corresponding CFD predictions. As in Figure 6, the data was cropped at  $z < -30$  mm and  $z > 30$  mm, and symmetry about the fuel jet center was assumed. The temperature map, shown by Figure 7(a), shows that CFD and experimental temperatures are nearly in agreement in the freestream. Both vary between 1050-1150 K and show a slightly warmer trend at the bottom of the duct. However, the experimental temperature map tends to be 30-50 K hotter than the CFD map, whereas the uncertainty in this cropped experimental temperature map is  $\pm 50$  K, with 95% confidence. The minimum fuel-plume temperature is somewhat cooler in the CFD (257 K) than in the experimental data (309 K). An obvious difference between the two results is that cold fuel plume has penetrated deeper into the flow in the CFD than in the experiment. This deeper penetration in the CFD appears to result in a steeper temperature gradient at the bottom of the jet compared to the experiment. This point is discussed further below.

Figure 7(b) shows a comparison between the  $N_2$  mole fraction predicted by CFD and that measured by CARS. The measured and computed mole fractions in the freestream agree for the most part within the measurement uncertainty. The center of the fuel plumes, marked by low values of  $N_2$  mole fraction, is about 10 mm lower in CFD

than in the CARS measurement. Furthermore, the CFD predicts an  $N_2$  mole fraction of 0.08 at the center of the fuel jet compared to 0.17 for the measurement – a significant difference of a factor of 2. This result implies that the CFD computation has underpredicted the mixing and overpredicted the penetration of the jet, confirming the observations made from the temperature map. Deeper penetration and less mixing of the fuel plume in the CFD compared to experiment are consistent because jet penetration generally trades off against mixing.

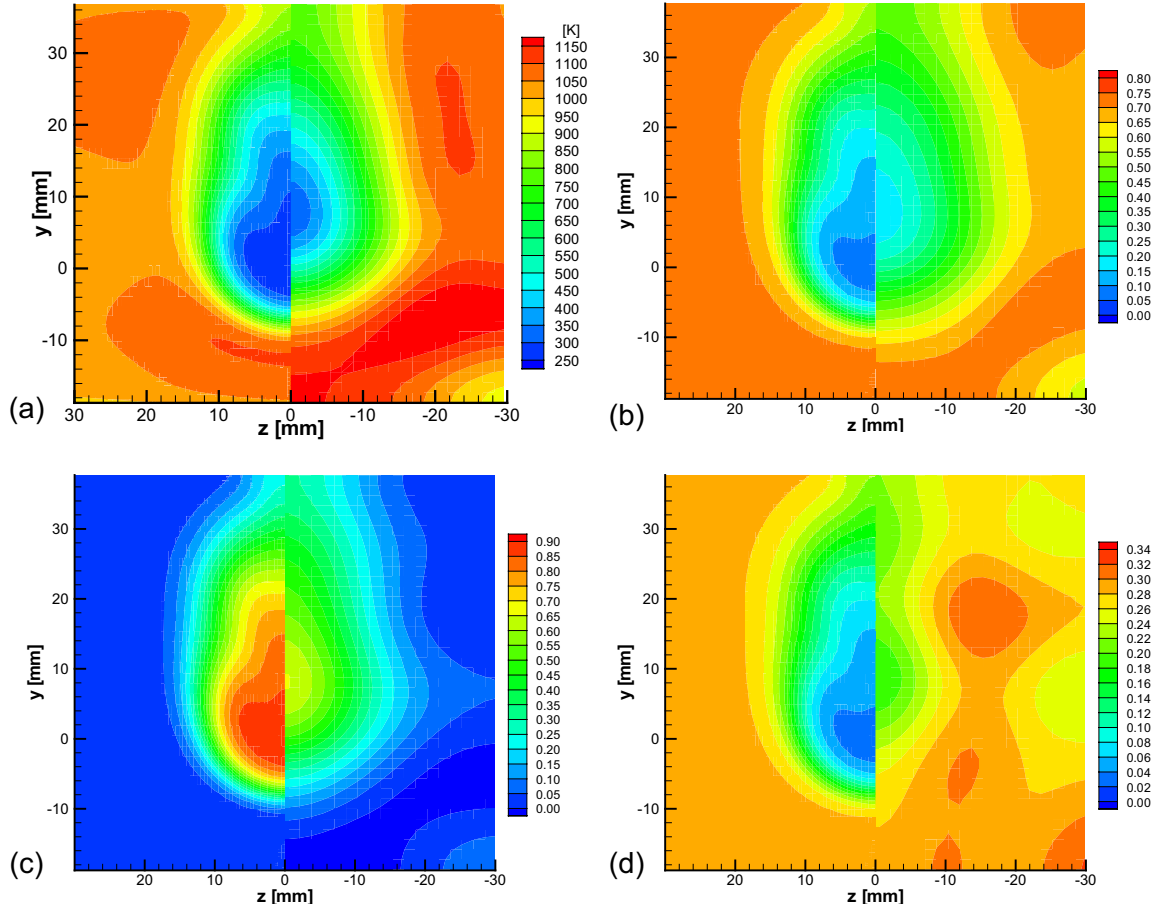


**Figure 7.** Comparison between CFD and measured mean temperature and species mole fraction maps: (a) temperature, (b)  $\chi_{N_2}$ , (c)  $\chi_{H_2}$ , and (d)  $\chi_{H_2O}$ .

Some interesting observations can be drawn from a comparison of  $H_2$  maps from CFD and the experiment, in Figure 7(c). First, the CFD predicts a higher mole fraction of  $H_2$  (up to 0.88) than the experiment (0.66). Furthermore, the extent of the hydrogen is larger in the CFD than in the experiment. In fact, the CFD map appears to contain a greater integrated flow rate of  $H_2$  than the experiment. This is unphysical. It may be that the CARS measurement of  $H_2$  is systematically low, consistent with flame measurements where the  $H_2$  mole fraction was found to be 10-15% lower than predicted. A possible solution to this problem is to investigate and improve the spectral modeling of  $H_2$ , thought to be the source of this systematic error. Another observation from the two  $H_2$  maps is that the measured fuel plume has an oval shape whereas the CFD fuel plume has a more complicated mushroom shape. This difference can be attributed to the use of 6<sup>th</sup> order fits to the data. These functions do not have sufficient curvature to pick up such fine detail in the data. A further comparison is that the bottom of the computed  $H_2$  fuel plume is much more steeply sloped than the measured fuel plume; this point is discussed in more detail below.

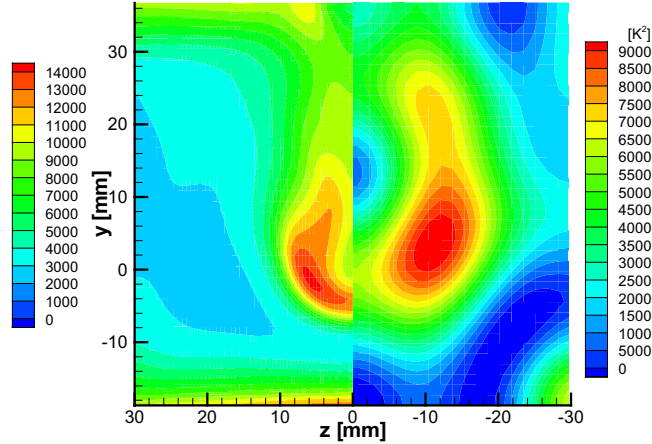


**Figure 8.** Comparison between CFD-predicted turbulence kinetic energy (left) and measured  $\langle T'T' \rangle$  map (right).

### Fluctuating Parameters

Figure 8 shows a comparison between two derived quantities: the turbulence kinetic energy (TKE), based on CFD, and the temperature variance, based on CARS measurements. While this is not a perfect comparison, both quantities are indicative of turbulent fluctuations. The two maps look qualitatively similar: non-fluctuating freestream gases on the outside and horse-shoe shaped turbulent regions around the bottom of the fuel plume. Furthermore, in both maps, the turbulence is more intense at the sides of the bottom of the fuel plume than on the bottom center of the fuel plume. However, the radius of peak ridge of maximum  $\langle T'T' \rangle$  values is twice as far from the center of the fuel plume than the corresponding peak TKE. This is a significant discrepancy: based on the turbulence intensity, it appears that the experimental fuel jet has a diameter that is twice as large as the CFD predicts. However, this is an apples-to-oranges comparison, so caution must be used when drawing conclusions from this comparison. One possible reason for this difference in radius could be that the fit order of the surface used to fit the  $\langle T'T' \rangle$  map was not high enough. However, using higher fit orders resulted in qualitatively similar maps with similar radii. So, this is not though to be a factor contributing to this discrepancy.

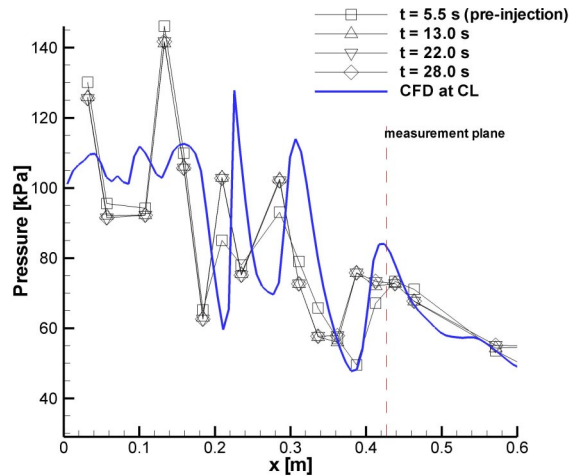


**Figure 9.** Measured and CFD-computed pressures.

### Pressure data.

A final point of comparison between the CFD and the experimental measurements is the static pressure. Figure 9 shows a plot of the measured and computed static pressures in the duct as a function of the distance downstream. The general trends are similar, but the shock positions in the CFD appear to be downstream of the experimentally measured positions by about 15-30 mm, the discrepancy increasing with distance down the duct.



## DISCUSSION

Figure 7(a) showed that near the bottom of the fuel plume the CARS temperature map changed more gradually, vertically through the mixing layer, compared to CFD. This discrepancy could either be caused by inaccurate CFD predictions or by misinterpretation of the CARS data by the response surface fits. To investigate whether the response surfaces can fit to gradients as steep as those predicted by CFD, we used the same functions used to fit the CARS data to fit a CFD-predicted temperature map. The CFD temperature map was interpolated onto a two-dimensional rectangular grid with a spacing of about 3 mm. Figure 10 shows a vertical centerline slice of the CFD along with three different fits, all of which use the 6<sup>th</sup>-order cosine series bivariate function. The fit to the entire 56-mm height of the duct shows significant discrepancies near the shear layer – on the order of 200 K or greater. Furthermore, in the response surface fit, the gradient of the shear layer near between  $y = -5$  and  $-10$  is clearly wrong. The CFD has a slope of 154 K/mm, while the fit has a slope of 58 K/mm: a difference of a factor 3.

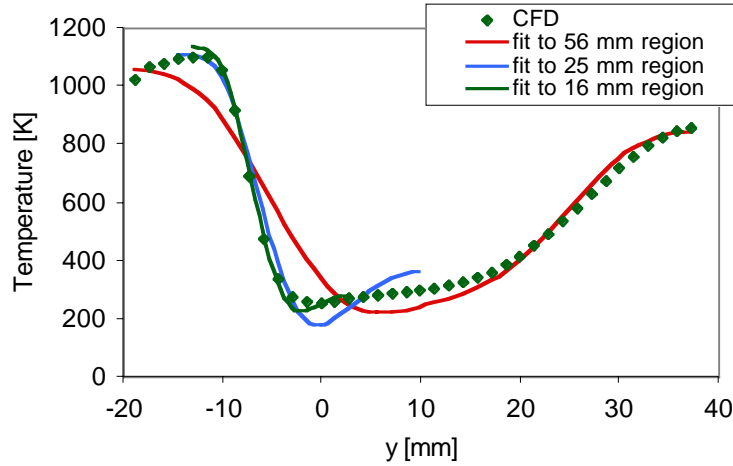


**Figure 10.** Comparison of three different response surface fits to a CFD-predicted temperature map. All three fits used the 6<sup>th</sup> order cosine series bivariate function, and fit over the spanwise range of  $-30 < z < 30$  and the vertical range shown in the figure.

One solution to this problem is to fit the data with higher-ordered functions, such as 7<sup>th</sup> or 8<sup>th</sup> order cosine series bivariate functions. Fitting the CFD temperature map with higher-ordered functions did improve the fit, but did not altogether remove this problem of wrongly fitting the slope. Another approach used previously,<sup>19,20</sup> is to fit to a smaller range of data, but with the same (or lower) fit order. This approach has been used in Figure 10, where fits over 25 and 16 mm, instead of the entire 56 mm height of the duct, were used. Fitting over 25 mm improves the estimation of the slope to 123 K/mm, while fitting over 16 mm brings the fitted slope into close agreement with the CFD: 152 K/mm. Thus, by fitting over a small enough range, gradients in the data that are as steep as the CFD gradient can be measured. It should be pointed out that both increasing fit order and fitting to a smaller range of data have negative consequences: both increase uncertainty in the fit and both degrade the statistical signal-to-noise ratio in the fit, as measured by the *Model F-statistic*.<sup>19,20</sup>

Since we have shown that fitting over a smaller data range can resolve gradients in the data that are as steep as the CFD predicts, it remains to be seen whether fitting the measured CARS data with a smaller range will result in a steeper slope in the shear layer. Figure 11 shows a comparison between the experimental data, CFD and two-response surface fits, both of which use the 6<sup>th</sup> order cosine series bivariate function. The blue response surface fit is that used to fit the entire 56 mm height of the duct while the green curve is the fit to a 16-mm subsection of the duct, near the shearlayer. In both cases, the fit includes data from  $-30 < z < 30$ .

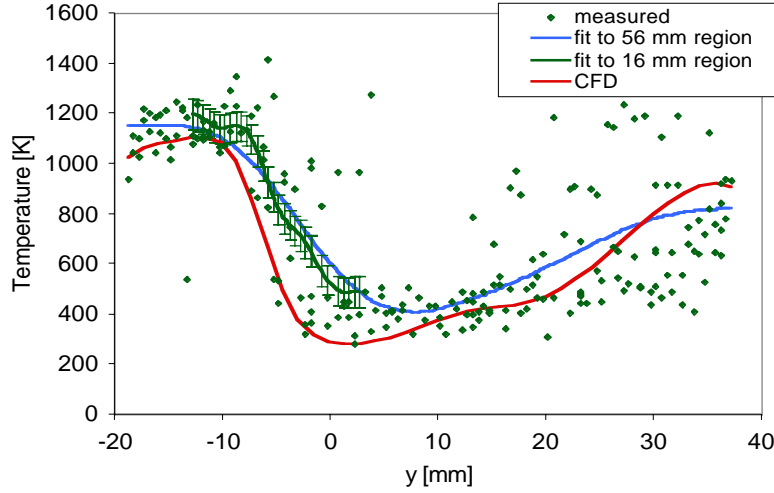


**Figure 11.** Measured vertical CARS temperature profile at  $z = 7$  mm, corresponding to the scan that was closest to the centerline of the fuel plume. Also shown are surface fits to the data plane between  $-30 < z < 30$  and the  $y$ -range shown above. The error bars are 95% confidence interval half widths. The CFD prediction at the same location is also shown.

A few observations about this figure can be made. First, the fit over the shorter  $y$ -range has a steeper slope than the fit to the larger  $y$ -range. In other words, the fit to the full height of the duct (shown in all of the previous figures in this paper) has blurred the shear layer at the bottom of the fuel plume and possibly elsewhere. By comparing the smaller- $y$ -range fit to the CFD, we can conclude that the CFD predicts that the bottom edge of the jet (as measured by the region between 600 and 800 K) penetrates about 3 mm, or 5% of the duct height, too far towards the floor of the duct, compared to the data. Furthermore, CFD predicts a steeper slope in the shear layer (128 K/mm) than the smaller- $y$ -range fit (71 K/mm). As mentioned above, these two effects are consistent with each other: less mixing (thinner shear layer) typically corresponds to more jet penetration. Based on this evidence, the CFD should be recomputed using a model that increases the mixing rate.

Note that the data at the right of Figure 11 corresponds to the upper portion of the duct in the temperature surface fit. The large variance in the measurements here are due to large turbulent fluctuations in the flowfield itself rather than measurement uncertainty. The region at the far left of the plot, in the freestream gas, provides a better indication of the temperature measurement uncertainty.

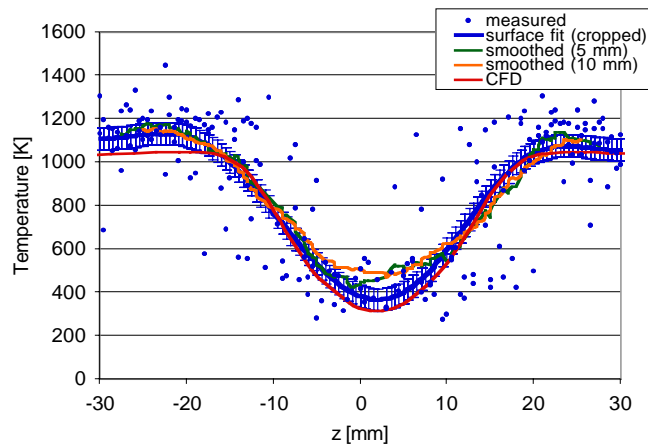


**Figure 12.** CARS temperatures measured with a horizontal scan through the flow at  $y = 13.2$  mm. Also shown are: the response surface fit, the CFD prediction, and two smoothed experimental data profiles. The response surface was fit to  $-30 < z < 30$  and  $-19 < y < 37$ . Spanwise symmetry was not assumed. The CFD was shifted by 2 mm in the  $+z$  direction to line up with the center of the plume. The error bars on the response surface fit indicate the 95% confidence interval half-width uncertainty levels.

Further comparisons can be made between the measured CARS data, the response surface fits and the CFD. Figure 12 shows a comparison for a horizontal cut through the flow at  $y = 13.2$  mm. This figure shows a sensible fit of the response surface to the data, and agreement between the surface fit and the CFD over much of the span. The CFD appears to be correctly predicting the width of the temperature profile at this height. Two other curves are also shown. These are experimental data that have been smoothed by a 'boxcar averaging' function. For example, the 5-mm smoothed curve computes each data point as the average of the raw data within  $\pm 2.5$  mm of that location. Using such a function allows estimation of the effective amount of smoothing associated with the response surface fits. The 5-mm smoothing curve is in reasonable agreement with the response surface data, while the 10-mm smoothing curve appears to be overly smoothed. Thus, as a rough indication of the amount of smoothing, the surface fits appear to effectively smooth the data equivalent to a 5-10 mm boxcar average smoothing function.

Whereas Figure 12 was chosen as an example where the CFD and the experiment agree, Figure 13 shows where they disagree. This height of the flow,  $y = -1.8$ , cuts through the center of the fuel jet in the CFD, but samples the mixing layer below the fuel plume in the experiment. The measurements show a wildly fluctuating flow in which gas temperatures between 300 K and 1200 K are almost equally probable over a width of about 30 mm. When this data is smoothed by a 5-mm boxcar averaging function it is generally in agreement with the response surface fit to the data. CFD, on the other hand, is far out of agreement. In the freestream, the CFD temperature is about 2 times outside the 95% confidence interval half width fit uncertainty; At the center of the fuel plume, the CFD is about 7 times outside the 95% confidence interval half widths. With certainty, we can state that the CFD and the experiment do not agree in this region.

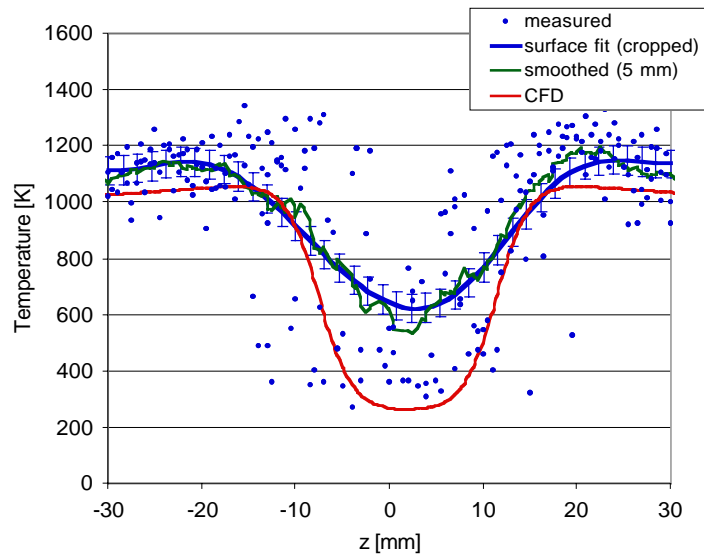


**Figure 13.** CARS temperatures measured with a horizontal scan through the flow at  $y = -1.8$  mm. Also shown are: the response surface fit, the CFD prediction, and one smoothed experimental data profile. The response surface was fit to  $-30 < z < 30$  and  $-19 < y < 37$ . Spanwise symmetry was not assumed. The CFD was shifted by 2 mm in the  $+z$  direction to line up with the center of the plume. The error bars on the response surface fit indicate the 95% confidence interval half-width uncertainty levels.

## CONCLUSIONS

We have used the dual-pump CARS measurement technique to simultaneously measure temperature and the mole fraction of  $N_2$ ,  $H_2$  and  $O_2$  in a model supersonic combustor for conditions where combustion has been inhibited. About 2300 single-shot measurements were obtained at  $\sim 1700$  different points in the flowfield. These measurements were fit with analytic surfaces to provide two-dimensional maps of the flow. The maps were used, together with the raw data, to compute fluctuating quantities and their correlations, including  $\langle T'T' \rangle$ ,  $\langle T'\chi_{H_2}' \rangle$ , and  $\langle \chi_{H_2}'\chi_{N_2}' \rangle$ , among others. This type of data should be useful for developing new models to predict turbulent flow and turbulent mixing. Furthermore, the raw data and the analytic maps have been compared with a preliminary CFD simulation of the flow. A detailed comparison indicated that the CFD predicted that the jet would penetrate about 3 mm, or 5% of the duct height, too far into the flow. The comparison also showed that the CFD predicted a factor of  $\sim 1.8$  steeper

temperature profile in the shear layer at the bottom of the fuel plume. It is expected that the CFD will be run again with models adjusted to increase the mixing.

The CARS system, analysis and application described above could be improved in several ways. First, the observed 10-15% systematic error in  $H_2$  mole fraction should be investigated because this error propagates during the analysis resulting in an overestimation of  $H_2O$  mole fraction in fuel-rich regions. Room temperature gas-cell experiments should be able to confirm this modeling error, and if confirmed, the spectral modeling of  $H_2$  would be carefully scrutinized. Second, a direct measurement of the  $H_2O$  mole fraction would be preferable to the inferential method currently used. Third, the combination of an injection seeded YAG laser and modeless dye laser could be used to improve the precision of all the measurements, perhaps by a factor of two or more. Fourth, more data could be acquired, which would allow the measured parameters to be determined more precisely and conclusions drawn more confidently. In the next set of measurements an axi-symmetric flowfield should be probed as this would allow far more precise determination of flow properties and their correlations with comparable sized data sets, removing the unnecessary complexities introduced by attempting to look at fundamental mixing processes in a confined combustor. Finally, the development of a velocity measurement technique that would operate simultaneously with the CARS method would greatly enhance the value of these experiments by providing much-needed correlations between velocities, temperatures and mole fractions.

### **ACKNOWLEDGEMENTS**

We wish to acknowledge the assistance of Diego Capriotti from NASA Langley Research Center for coordinating the running of the facility and processing of pressure data for this paper. Also, Jeff White from NASA Langley Research Center for helping compute libraries of CARS spectra on a large cluster of personal computers, significantly decreasing the computational time.

### **REFERENCES**

- 
- 1 B Shirinzadeh, M. E. Hillard, R. J. Balla, I. A. Waitz, J. B. Anders, R. J. Exton "Planar Rayleigh-scattering results in helium-air mixing experiments in a Mach-6 wind-tunnel", *Applied Optics* v. 31 (30), p. 6529-6534, Oct. 20 1992.
  - 2 I. A. Waitz, F. E. Marble, E. E. Zukoski, "Investigation of a contoured wall injector for hypervelocity mixing augmentation", *AIAA J*, v. 31 (6), p. 1014-1021, Jun. 1993.
  - 3 N. T. Clemens, M. G. Mungal, "Large-scale structure and entrainment in the supersonic mixing layer", *J Fluid Mech* 284, p. 171-216, Feb. 10 1995.
  - 4 J.M. Donohue and J.C. McDaniel, "Complete three-dimensional multiparameter mapping of a supersonic ramp fuel injector flowfield", *AIAA J* v. 34 (3), p. 455-462, Mar. 1996.
  - 5 T. C. Island, W. D. Urban, M. G. Mungal, "Mixing enhancement in compressible shear layers via sub-boundary layer disturbances", *Phys. Fluids* 10 (4), p. 1008-1020 Apr. 1998.
  - 6 J. S. Fox, A. F. P. Houwing, P. M. Danehy, M. J. Gaston, N. R. Mudford, and S. L. Gai, "Mole-fraction-sensitive imaging of hypermixing shear layers", *J. of Propulsion And Power*, v. 17(2), Mar.-Apr. 2001
  - 7 A. D. Cutler, G. S. Diskin, P. M. Danehy, J. P. Drummond, "Fundamental mixing and combustion experiments for propelled hypersonic flight," *AIAA Paper* 2002-3879, 38th AIAA/ASME/SAE/ASEE Joint Propulsion Conference and Exhibit, Indianapolis, Indiana, Jul. 7-10, 2002.
  - 8 J. A. White, "Diagnostic Measurements for Modeling Turbulent Combustion in Scramjets Operating in the Dual-Mode Regime", *JANNAF APS/CS/PSHS/MSS Joint Meeting*, Dec. 1-5, Colorado Springs, CO, 2003.
  - 9 P.E. Dimotakis "Turbulent Free Shear Layer Mixing and Combustion," in Murthy, S.N.B., Curran E.T. (eds), *High-Speed Flight Propulsion Systems*, AIAA Progress in Astronautics and Aeronautics Series, Vol.137, Washington D.C., 1991, pp. 265-340.
  - 10 R. P. Lucht, "Three-Laser Coherent Anti-Stokes Raman Scattering Measurements of Two Species," *Opt. Lett.* 12, pp. 78-80, 1987.
  - 11 R.D. Hancock, F.R. Schauer, R.P. Lucht, R.L. Farrow, "Dual-pump CARS measurements of nitrogen and oxygen in a laminar jet diffusion flame," *Appl. Opt.* 36, pp. 3217-3226, 1997.

- 
- 12 For a more complete discussion about CARS, see A. C. Eckbreth, *Laser Diagnostics for Combustion Temperature and Species* (2nd Edition), Gordon and Breach Publishers, Amsterdam, The Netherlands, 1996.
  - 13 A. D. Cutler, P. M. Danehy, R. R. Springer, S. O'Byrne, D. P. Capriotti and R. DeLoach, "CARS thermometry in a Supersonic Combustor for CFD Code Validation", *AIAA Journal*, in press.
  - 14 R. R. Springer, A. D. Cutler, G. S. Diskin, M. W. Smith, "Conventional/Laser Diagnostics to Assess Flow Quality in a Combustion-Heated Facility," *AIAA Paper 99-2170*, 35th AIAA/ASME/SAE/ASEE Joint Propulsion Conference and Exhibit, Los Angeles, CA, June 20-24, 1999.
  - 15 S. O'Byrne, P. M. Danehy, A. D. Cutler, "N<sub>2</sub>/O<sub>2</sub>/H<sub>2</sub> Dual-pump CARS: validation experiments," 20th International Congress on Instrumentation in Aerospace Simulation Facilities, Goettingen, Germany, August, 2003.
  - 16 Palmer, R. E., *The CARSFT Computer Code for Calculating Coherent Anti-Stokes Raman Spectra: User and Programmer Information*, Sandia National Laboratories Report SAND89-8206, Livermore, California, 1989.
  - 17 J. J. More, B. S. Garbow, and K. E. Hillstrom, "User Guide for MINPACK", ANL-80-74, Aug, 1980.
  - 18 R. P. Lucht, V. V. Natarajan, C. D. Carter, K. D. Grinstead Jr., J. R. Gord, P. M. Danehy, G. J. Fiechtner, R. L. Farrow, "Dual-pump coherent anti-Stokes Raman scattering temperature and CO<sub>2</sub> concentration measurements," *AIAA Journal*, 41, pp. 679-686, 2003.
  - 19 P.M. Danehy, R. DeLoach, A.D. Cutler, "Application of Modern Design of Experiments to CARS Thermometry in a Supersonic Combustor", *AIAA Paper 2002-2914*, June 2002.
  - 20 P. M. Danehy, A. A. Dorrington, A. D. Cutler, R. DeLoach, "Response Surface Methods for Spatially-Resolved Optical Measurement Techniques", *AIAA Ground Testing Conference*, Reno NV, *AIAA Paper 2003-0648*, January 2003.
  - 21 Rodriguez, C.G., and Cutler, A.D., "CFD Analysis of the SCHOLAR Scramjet Model", *AIAA Paper 2003- 7039*, to be presented at the 12th International Space Planes and Hypersonic Systems and Technologies Conference, Norfolk, Virginia, 15-18 December 2003.
  - 22 White, J.A., and Morrison, J.H., "A Pseudo-Temporal Multi-Grid Relaxation Scheme for Solving the Parabolized Navier-Stokes Equations", *AIAA 99-3360*, 1999.
  - 23 Edwards, J.R., "A Low-Diffusion Flux-Splitting Scheme for Navier-Stokes Calculations", *Computers and Fluids*, Vol. 26, No. 6, 1997, pp. 635-659.
  - 24 Pulliam, T.H., and Chaussee, D.S., "A Diagonal Form of an Implicit Approximate-Factorization Algorithm", *Journal of Computational Physics*, Vol. 39, Feb. 1981, pp. 347-363.
  - 25 Wilcox, D.C., *Turbulence Modeling for CFD*, 2nd. Edition, DCW Industries, Inc., 1998.
  - 26 A. Thumann, T. Seeger, A. Leipertz, "Evaluation of 2 different gas temperatures and their volumetric fraction from broad-band N<sub>2</sub> coherent anti-Stokes-Raman Spectroscopy spectra", *Applied Optics*, v. 34 (18), p. 3313-3317 Jun. 20 1995.
  - 27 G. E. P. Box and N. R. Draper, "Empirical Model-Building and Response Surfaces", Wiley, 1987.